Evaluating and Optimizing Control Algorithms for Combined LGS/NGS MCAO Systems (draft 2.0)

Brent Ellerbroek

20 April 2000

1 Introduction and Summary

As described previously, the Gemini-South MCAO system uses wave front sensor measurements from a combination of natural- and laser guide stars (NGS and LGS) to determine the distribution of atmospheric turbulence in three dimensions and compensate the associated wave front aberrations across an extended field-of-view. The NGS tip/tilt measurements are necessary to measure tilt and tilt anisoplantism modes in the atmosphere which cannot be detected using laser guide stars. The LGS and NGS measurements can be viewed as components of an overall WFS measurement vector, but they are very different in several important characteristics. The LGS measurements are (i) very high order, (ii) high SNR, and (iii) associated with a fixed guide star geometry. The NGS measurements are (i) very low order, (ii) high-to-low SNR depending upon the science field, and (iii) associated with a field-dependent guide star geometry. For improved performance, the MCAO control algorithm must account for the field-dependent configuration of the natural guide stars. For efficient implementation, it would be best if the LGS component of the algorithm could remain fixed. This report describes and evaluates a partially decoupled control algorithm which satisfies these requirements.

These issues for the MCAO control system present several analogies with conventional LGS AO. Existing LGS AO control systems already incorporate a higher-order control loop including the LGS wave front sensor (WFS) and a deformable mirror (DM), and a low-order control loop including the tip/tilt NGS WFS and a tip/tilt mirror (TTM). The two loops are largely but not entirely decoupled. The overall tip/tilt component of the LGS WFS measurement is unreliable due to LGS position uncertainty, and is projected out of the reconstructed wave front estimate before it is applied to the DM. To first order, the higher-order LGS loop is insensitive to the atmospheric tip/tilt disturbance and the correction applied by the TTM. Higher-order wavefront aberations *do* couple into the low-order tip/tilt loop (e.g., coma couples into the tilt estimate obtained from a centroid or quadrant detector measurement), but with the higher-order loop closed the residual aberrations are small enough that this is generally not a significant error source. The control bandwidths for the two loops can be optimized independently as a function of (i) the PSD's for the separate input disturbances and (ii) the SNR's for the LGS and NGS WFS's.

All of these points apply equally to the proposed MCAO control system, but some extensions are required. The low-order NGS control loop now corrects five modes which are unsensed or poorly sensed by the LGS measurements, and three of these modes associated with tilt anisoplanatism are corrected via the multiple DM's. Summing the LGS and NGS contributions to the DM commands is an electronics implementation issue considered elsewhere, but this complication for MCAO will only result in loop cross-coupling due to hardware imperfections (e.g., hysteresis) which will not be considered further at the CoDR level. The control problem for each of the NGS control loop is potentially richer, with distinct PSD's for the 5 modes and varying SNR's for each of the 3 NGS. It may even be desirable to redefine the modes themselves for each science field, depending upon the wind profile and the configuration and brightness of the guide stars. As with conventional LGS AO, residual higher-order aberrations left uncorrected by the LGS control loop will again couple into the NGS tip/tilt measurements.

The remainder of this report describes our approach to evaluating and optimizing partially decoupled MCAO control algorithms. Section 2 begins with an expression for the aperture- and field-averaged phase variance in an MCAO system as a function of the input phase disturbance and the DM actuator commands, and then describes a coordinate transformation to simplify this expression into the sum of (i) a fitting error term for optimal DM commands, and (ii) the square of the distance between the optimal and actual DM command vector. This representation for the phase variance simplifies the algebra involved in evaluating and optimizing wave front control algorithms in the remainder of the report.

Section 3 considers "nodal" control algorithms which reconstruct an estimate of the current closed-loop wave front via a matrix multiply, and then temporally filter this estimate using the same control law for all DM degrees-of-freedom. In general, the temporal dynamics of even this simple algorithm are a highly nonlinear function of the coefficients of the reconstruction matrix E, unless this matrix is assumed to be a left inverse of the DM-to-WFS influence matrix G. In this special case the closed-loop DM commands become a linear function of the coefficients of E, and the overall performance of the AO control loop can be evaluated and optimized using least squares methods. This evaluation includes the effects of (i) DM/WFS fitting error, (ii) WFS noise, (iii) control loop servo lag, (iv) general anisoplanatism, and (v) LGS tip/tilt uncertainty, but does not include higher-order effects such a diffraction, scintillation, or nonlinearities in the AO system components.

Section 4 extends these results to a form of modal control. The standard formulation of modal control assumes a fixed basis of orthonormal wave front control modes, such as Zernikes, and optimizes the control bandwidth for each mode to minimize the combined error due to sensor noise and servo lag. The approach taken here optimizes both the control bandwidths and the choice of orthonomal modal basis, since for MCAO it seems very possible that the preferred choice of modes may depend upon the locations and magnitudes of the natural guide stars. Determining the best modal basis for an n-dimensional space of DM actuator commands requires a nonlinear optimization over the set of n-dimensional unitary matrices. This would be impractical for the full space of DM actuator commands with n on the order of 1000, but is acceptable for the $n = 5$ dimensional subspace controlled by the NGS WFS measurements.

The methods described in sections 3 and 4 for modeling closed-loop AO systems have been presented previously [1, 2], but the notation used here is new (and we hope a little clearer).

Section 5 shows how the "nodal" and modal algorithms presented in sections 3 and 4 can be combined into a partially decoupled NGS/LGS MCAO control algorithm. With proper selection of the NGS- and LGS-controlled subspaces and/or preprocessing of the LGS WFS measurements to project off the influence of the NGS-controlled modes, the LGS control loop can be entirely decoupled from the behavior of the NGS loop. The LGS control algorithm can be optimized and evaluated independently. The modal NGS control algorithm is determined as a second step, with the residual errors in the LGS loop acting as a source of correlated noise in the NGS measurements. Section 5 presents two possible approaches for defining the NGS- and LGS-controlled subspaces. How to analytically determine the optimal decomposition is not yet clear.

Section 6 presents sample numerical results on NGS modal control. To reduce computation requirements, we have considered a MCAO system of slightly lower order than is proposed for Gemini-South (12×12 supertures per LGS WFS as opposed to 16×16), but the remainder of the system and atmospheric parameters are highly comparable. We find that for a favorable NGS constellation of three well spaced guide stars of equal magnitude, the NGS magnitude limit for a 50% Strehl ratio reduction in H band is in the range from 18.6 to 19.2, depending upon sky brightness. These results include the effect of windshake-induced tip/tilt jitter for a preliminary jitter PSD taken from Gemini-North. Reducing the separations between the three NGS from 0.87 to 0.43 arc minutes yields limiting magnitudes in the range from 18.1–18.5 for a centered constellation, and in the range 17.9–18.2 for a constellation displaced to one side of the science field. Additional calculations for a larger range of NGS constellations and atmospheric conditions are necessary, but these initial results suggest that MCAO sky coverage will be large enough to be scientifically useful.

Finally, Section 7 is a summary of key conclusions and possible future work.

2 MCAO Figure-of-Merit

The purpose of the MCAO system is to compensate a turbulence-induced phase distortion profile by applying the correct actuator commands to several deformable mirrors. The phase profile $\phi = \phi(r, \theta)$ is a function of telescope aperture coordinates r and the direction of the source θ. The set of actuator commands for all deformable mirrors will be represented as the vector a. The instantaneous figure-of-merit for the MCAO system is the mean-square residual phase error remaining after the DM correction. This phase variance is denoted σ^2 and is described by the formula

$$\begin{aligned} \sigma^2 &= \sigma^2(\phi, a) \\ &= \iint dr\, d\theta\, W_a(r) W_f(\theta) \left\{ \left[\phi(r,\theta) - \bar{\phi}(\theta)\right] - \sum_i a_i \left[h_i(r,\theta) - \bar{h}_i(\theta)\right] \right\}^2 . \end{aligned} \tag{2-1}$$

Here $W_a(r)$ is weighting function defining the telescope aperture, $W_f(\theta)$ is a weighting function defining the desired field-of-view, $h_i(r, \theta)$ is the influence function for actuator number i, and the aperture-averaged value $\bar{g}(\theta)$ of a function $g(r, \theta)$ is defined by the equation

$$\bar{g}(\theta) = \int dr W_a(r) g(r, \theta) \tag{2-2}$$

(For simplicity, it is assumed that the integrated values of $W_a(r)$ and $W_f(\theta)$ equal unity). Eq. (2-1) assumes that each DM figure can be computed using linear superposition of the individual actuator influence functions. The aperture-averaged values of the input phase distortion and the DM correction are subtracted before computing the variance, because the overall piston component of the wavefront will have no effect upon image quality. The actuator influence functions h_i will depend upon θ for deformable mirrors which are not optically conjugate to the pupil plane of the telescope. The weighting functions $W_a(r)$ and $W_f(\theta)$ can take any nonnegative real values, although the aperture function W_a is typically $\{0, 1\}$-valued. For practical problems, the integrals in Eq. (2-1) must be evaluated numerically as sums over discrete points.

The remainder of this section transforms Eq. (2-1) into a form which is more agreeable for linear systems modeling of MCAO systems. Expanding the square and interchanging the order of summation and integration yields the result

$$\sigma^2 = \sigma_0^2 - 2a^T v + a^T W a, \tag{2-3}$$

where the scalar σ_0^2, vector v, and matrix W are abbreviations for the integrals

$$\sigma_0^2 = \iint dr\, d\theta\, W_a(r) W_f(\theta) \left[\phi(r,\theta) - \bar{\phi}(\theta)\right]^2 , \tag{2-4}$$

$$v_{(i)} = \iint dr\, d\theta\, W_a(r) W_f(\theta) \left[\phi(r,\theta) - \bar{\phi}(\theta)\right] \left[h_i(r,\theta) - \bar{h}_i(\theta)\right] , \tag{2-5}$$

$$W_{(i,j)} = \iint dr\, d\theta\, W_a(r) W_f(\theta) \left[h_i(r,\theta) - \bar{h}_i(\theta)\right] \left[h_j(r,\theta) - \bar{h}_j(\theta)\right] . \tag{2-6}$$

(Note that in this report we will use parenthesized subscripts to refer to the components of vectors or matrices, while subscripts without parenthesis denote elements of a series of vectors or matrices. The superscript T denotes the transpose operator for vectors and matrices.)

Eq. (2-3) clarifies that phase variance σ^2 is a quadratic function of the DM actuator command vector a. The matrix algebra in the following sections can be simplified if the actuator cross-coupling matrix W can be reduced to the identity. Since W is symmetric positive semidefinite, its eigenvalue-eigevector decomposition takes the form

$$W = U \Lambda U^T, \tag{2-7}$$

where U is a unitary matrix (i.e., $UU^T = U^T U = I$, the identity matrix), and Λ is a diagonal matrix with nonnegative real elements. We will assume that W is actually symmetric positive definite, so that all

diagonal elements of Λ are positive[1] In this case, it is convenient to represent the DM actuator commands and input phase distortion using the coordinate transformations

$$c = \Lambda^{1/2} U^T a, \tag{2-8}$$

$$x = \Lambda^{-1/2} U^T v. \tag{2-9}$$

Substituting these tranformations into Eq. (2-3) and completing the square yields the formula

$$\begin{aligned} \sigma^2 &= \sigma_0^2 - 2c^T x + c^T c \\ &= (\sigma_0^2 - x^T x) + ||x - c||^2 \end{aligned} \tag{2-10}$$

for the value of the instantaneous mean-square phase variance σ. In this new basis, the vector x is the best-fit set of DM actuator commands for the input phase distortion profile, and can be considered a finite dimensional representation of ϕ. The term within parenthesis in Eq. (2-10) is the fitting error due to higher-order modes orthogonal to this representation. The second term in this equation is due to the error in selecting the DM actuator command vector c. This error is a function of the MCAO control algorithm, as investigated in the remainder of this report.

3 Nodal Control

The adjective "nodal" is used here to denote the class of AO control algorithms illustrated in Fig. (1). This approach estimates the instantaneous closed-loop wave-front error from closed-loop WFS measurements via a fixed matrix multiply, and then temporally filters this estimate using the same control law for all DM degrees-of-freedom. The control algorithm is represented in the frequency domain by the equation

$$c(\nu) = k(\nu) E[s(\nu) - Gc(\nu)], \tag{3-1}$$

where ν is the temporal frequency variable, $k(\nu)$ is the scalar control law, E is the wave front reconstruction matrix, $s(\nu)$ is the open-loop WFS measurement, and G is the DM-to-WFS influence matrix. The WFS measurement vector $s(\nu)$ can include components from multiple sensors, and includes the effects of measurement noise and LGS position uncertainty.[2] Solving for $c(\nu)$ yields the result

$$c(\nu) = [I + k(\nu) EG]^{-1} k(\nu) E s(\nu). \tag{3-2}$$

The actuator command vector $c(\nu)$ is a nonlinear function of the coefficients of E due to the feedback of the control loop, and it is unclear whether Eq. (3-2) can be effectively used to evaluate and optimize the performance of high-order AO system.

One approach to futher progress is to assume that the reconstruction matrix E must satisfy the constraint

$$EG = I, \tag{3-3}$$

where I is the identity matrix. In this case Eq. (3-2) simplifies to the form

$$c = Ey, \tag{3-4}$$

where the function $y(\nu)$ is related to the open-loop WFS measurement vector $s(\nu)$ by the equation

$$y(\nu) = \left[\frac{k(\nu)}{1 + k(\nu)} \right] s(\nu). \tag{3-5}$$

The term within square brackets can be recognized as the closed-loop transfer fuction associated with the open-loop transfer function $k(\nu)$. Heuristically, Eq.'s (3-4) and (3-5) illustrate how the constraint in Eq. (3-3) has separated the spatial and temporal aspects of the wave front control problem.

[1] Otherwise, there are some linear combinations of DM actuator commands which do not change wave front quality at all. We can restrict the command vector a to a linear subspace excluding such commands without increasing the value of σ or degrading the performance of the control loop.

[2] The latter may be modelled by either adding additional correlated noise to s or projecting off the full-aperture tip and tilt components of WFS measurement.

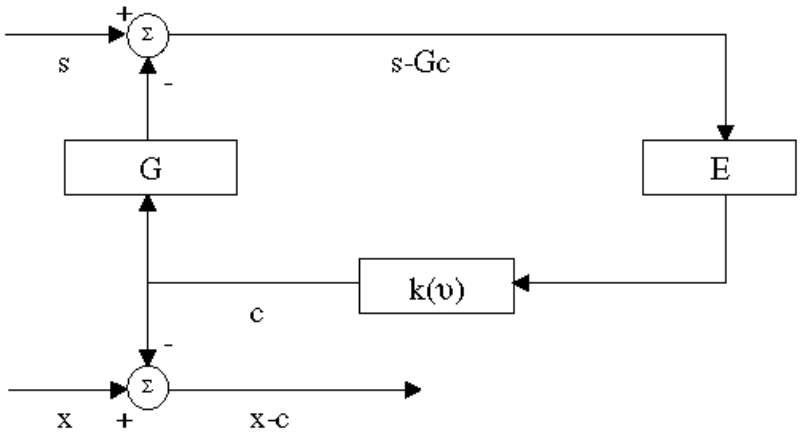

Figure 1: Nodal Control Block Diagram

Here x is a representation of the input phase distortion profile in terms of DM acuator commands, s is the open-loop WFS measurement vector, c is the DM acutuator command vector, E is the wave front reconstruction matrix, $k(\nu)$ is a scalar-valued temporal filter, and G is the DM-to-WFS influence matrix.

3.1 Evaluating Nodal Control

It is now possible to evaluate the expected value of the phase variance σ^2 for any reconstruction matrix E satisfying Eq. (3-3). Substituting Eq¿ (3-4) into Eq. (2-10) yields

$$\sigma^2 = (\sigma_0^2 - x^T x) + ||x - Ey||^2 \tag{3-6}$$

We will use the notation $\langle \cdots \rangle$ to denote ensemble averaging over the statistics of atmospheric turbulence, wind, and WFS measurement noise. Expressing the second term in Eq. (3-6) as $(x - Ey)^T(x - Ey)$ allows the expected value of σ^2 to be written as

$$\begin{aligned} \langle \sigma^2 \rangle &= (\langle \sigma_0^2 \rangle - \langle x^T x \rangle) + \langle x^T x \rangle - 2 \langle x^T E y \rangle + \langle y^T E^T E y \rangle \\ &= (\langle \sigma_0^2 \rangle - \langle x^T x \rangle) + \mathrm{trace}(\langle x x^T \rangle) - \mathrm{trace}(2E \langle y x^T \rangle) + \mathrm{trace}(E \langle y y^T \rangle E^T) \\ &= \sigma_f^2 + \mathrm{trace}(A - 2EB^T + ECE^T), \end{aligned} \tag{3-7}$$

where the terms σ_f^2, A, B, and C are abbreviations for the expressions

$$\sigma_f^2 = \langle \sigma_0^2 \rangle - \langle x^T x \rangle , \tag{3-8}$$

$$A = \langle x x^T \rangle , \tag{3-9}$$

$$B = \langle x y^T \rangle , \tag{3-10}$$

$$C = \langle y y^T \rangle . \tag{3-11}$$

The term σ_f^2 is the mean-square fitting error due to wave front modes orthogonal to the DM actuator commands, while the matrices A, B, and C describe the second-order statistics of the best-fit DM command vector x and the temporally filtered open-loop WFS measurement vector y. Computational methods for evaluating these covariances have been presented previously [1].

3.2 Optimizing Nodal Control

It is naturally of interest to determine the minimum value of $\langle \sigma^2 \rangle$ for a given set of AO system and atmospheric parameters. The optimized phase variance σ_*^2 and the associated optimal reconstruction matrix E_* are defined by the expressions

$$\sigma_*^2 = \min_E \langle \sigma^2 \rangle , \tag{3-12}$$

$$E_* = \arg\min_E \langle \sigma^2 \rangle , \tag{3-13}$$

where the minimum is taken over all matrices E satisfying the $EG = I$ constraint. Eq. (3-7) for $\langle \sigma^2 \rangle$ is quadradic in the coefficients of E, and the $EG = I$ constraint is linear. Using Lagrange multiplier techniques, the value of E_* can be obtained by solving the system of equations

$$-2B + 2E_*C = \Lambda G^T, \tag{3-14}$$

$$E_*G = I. \tag{3-15}$$

The left-hand-side of Eq. (3-14) are the partial derivatives of $\langle \sigma^2 \rangle$ with respect to the coefficients of E evaluated at E_*, and the right-hand-side is a linear combination of the derivatives of EG with respect to E.[3] The solution is given by the expression

$$E_* = BC^{-1} + (I - BC^{-1}G)(G^TC^{-1}G)^{-1}G^TC^{-1}, \tag{3-16}$$

which upon substitution back into Eq. (3-7) yields the result

$$\sigma_*^2 = \sigma_f^2 + A - BC^{-1}B^T + (I - BC^{-1}G)(G^TC^{-1}G)^{-1}(I - BC^{-1}G)^T. \tag{3-17}$$

The first term in Eq. (3-16) and the first three terms in Eq. (3-17) are the familiar formulas for minimizing $\langle \sigma^2 \rangle$ without the $EG = I$ constraint. The final term in each equation is the correction necessary to meet this condition. The size of these terms depend upon the magnitude of $I - BC^{-1}G$, which is simply the failure of the uncontrained estimator $E_0 = BC^{-1}$ to satisfy $E_0G = I$.

It should be noted that E_* has been computed for a particular value of the temporal filter $k(\nu)$, and that a second, nonlinear optimization over the parameters defining this filter is still necessary to determine optimal AO performance. This second step can be interpreted as balancing the competing effects of servo lag and WFS measurement noise. Finally, it should also be noted that the $EG = I$ constraint implies that null(G), the nullspace of the DM-to-WFS influence matrix G, consists of only the zero vector, and therefore every DM actuator command is uniquely identified by its (noise-free) effect on the WFS measurement vector. If null(G) is nontrivial we can proceed by restricting the DM actuator commands to a complementary subspace. *Which* complementary subspace to select for optimal AO performance cannot be determined analytically at this time, but for practical purposes good results are achieved by "slaving" selected edge actuators to follow a linear combination of the commands applied to their nearest neighbors. This reduces the dimension of the DM actuator command space by removing actuators corresponding to weak columns of G.

4 Modal Control

Modal control enables different components, or modes, of the wave front distortion profile to be compensated with different control bandwidths, depending upon the power spectrum of the disturbance and the WFS SNR. This more sophisticated approach will probably be necessary to obtain satisfactory MCAO performance with faint natural guide stars. Fig. 2 illustrates the conceptual formulation of modal control used in this report. The overall wavefront wave front distortion profile is first estimated m times by distinct or identical reconstruction matrices $E_1, \ldots, E_m$. The modal components of the wave front are then determined by

[3] The coefficients of Λ are the Lagrange multipliers and have nothing to do with the diagonal eigenvalue matrix in Eq. (2-7).

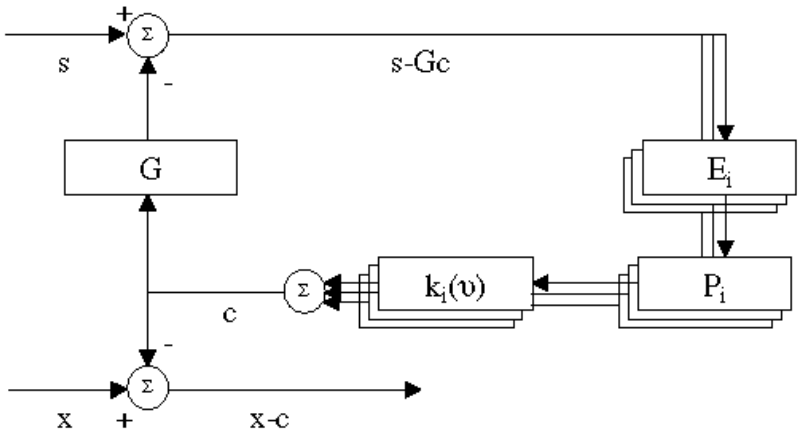

Figure 2: Modal Control Block Diagram

This figure is similar to Fig. 1, except that separate components of the wave front distortion are compensated using distinct reconstruction matrices E_i and temporal filters $k_i(\nu)$. The matrices P_i are the orthogonal projection operators onto these components.

applying m orthogonal projection operators $P_1, \ldots, P_m$ to the estimated wave fronts. For a complete, orthonomal basis of modes these projections will satisfy the conditions

$$\sum_i P_i = I, \tag{4-1}$$

$$P_i^T = P_i, \tag{4-2}$$

$$P_i P_j = \delta_{ij} P_i, \tag{4-3}$$

where δ_{ij} is the Kronecker delta function. The modal estimates are then temporally filtered by m control laws $k_1(\nu)$, ...,$k_m(\nu)$, and the filter outputs are summed and the result applied to the deformable mirrors. The option $k_i(\nu) \equiv 0$ for some particular i is allowed.

Standard modal control as used in the ADONIS, PUEO, and Hokupa'a AO systems corresponds to using a common reconstruction matrix for all E_i, and choosing projection operators P_i associated with Zernike modes. Of course, implementing modal control explicitly as illustrated in Fig. 2 would be terribly inefficient from a signal processing perspective, but this representation is useful for evaluating and optimizing the performance of the algorithm.

4.1 Evaluating Modal Performance

Proceeding as in the nodal case, the control law corresponding to Fig. 2 is the equation

$$c(\nu) = \sum_i k_i(\nu) P_i E_i [s(\nu) - Gc(\nu)], \tag{4-4}$$

which can be solved for $c(\nu)$ with the result

$$c(\nu) = \left[I + \sum_i k_i(\nu) P_i E_i G \right]^{-1} \sum_j k_j(\nu) P_j E_j s(\nu). \tag{4-5}$$

This is again a nonlinear function of the coefficients of E_i, and we restrict attention to reconstruction matrices satisfying the constraint

$$E_i G = I. \tag{4-6}$$

Substituting this condition into Eq. (4-5) yields

$$c(\nu) = \left[I + \sum_i k_i(\nu) P_i \right]^{-1} \sum_j k_j(\nu) P_j E_j s(\nu). \tag{4-7}$$

Using Eq.'s (4-1)–(4-3), the inverse in this expression may be written in the form

$$\left[I + \sum_i k_i(\nu) P_i \right]^{-1} = \sum_i [1 + k_i(\nu)]^{-1} P_i. \tag{4-8}$$

Substituting Eq. (4-8) into Eq. (4-7) and again applying Eq. (4-3) yields

$$c = \sum_i P_i E_i y_i, \tag{4-9}$$

where the filtered WFS measurements $y_i(\nu)$ are defined as

$$y_i(\nu) = \left[\frac{k_i(\nu)}{1 + k_i(\nu)} \right] s(\nu). \tag{4-10}$$

A comparison of this result with Eq.'s (3-4) and (3-5) confirms that nodal control is a trivial special case of modal control.

Eq. (4-9) can now be used to determine the expected mean-square phase error for a modal control system. Substituting this result into Eq. (2-10) and taking the expected value of both sides yields

$$\begin{aligned} \left\langle \sigma^2 \right\rangle &= \left(\left\langle \sigma_0^2 \right\rangle - \left\langle x^T x \right\rangle \right) + \left\langle \left|\left| x - \sum_i P_i E_i y_i \right|\right|^2 \right\rangle \\ &= \left(\left\langle \sigma_0^2 \right\rangle - \left\langle x^T x \right\rangle \right) + \left\langle \left|\left| \sum_i P_i (x - E_i y_i) \right|\right|^2 \right\rangle \\ &= \sigma_f^2 + \sum_i \sum_j \mathrm{trace} \left[P_i (A - E_i B_i^T - B_j E_j^T + E_i C_{ij} E_j^T) P_j^T \right]. \end{aligned} \tag{4-11}$$

Here σ_f^2 and A are as defined by Eq.'s (3-8) and (3-9), and B_i and C_{ij} are defined as the covariance matrices

$$B_i = \left\langle x y_i^T \right\rangle, \tag{4-12}$$

$$C_{ij} = \left\langle y_i y_j^T \right\rangle. \tag{4-13}$$

Given Eq.'s (4-2)–(4-3) and the fact that $\mathrm{trace}(MN) = \mathrm{trace}(NM)$ for any two correctly dimensioned matrices M and N, the terms in the final summation of Eq. (4-11) with $i \neq j$ are equal to 0. Eq. (4-11) therefore becomes

$$\left\langle \sigma^2 \right\rangle = \sigma_f^2 + \sum_i \mathrm{trace}(P_i M_i P_i^T) \tag{4-14}$$

where the matrix M_i is defined by the expression

$$M_i = A - E_i B_i^T - B_i E_i^T + E_i C_{ii} E_i^T \tag{4-15}$$

Eq. (4-14) is the basic result for evaluating modal control performance in terms of an expected mean-square phase error. It is worth noting that evaluating the complete second-order statistics of the residual phase errors, $\left\langle (x - c)(x - c)^T \right\rangle$, is more computationally intensive. For this calculation the double sum in the analog to Eq. (4-11) does not reduce to a single sum, and all of the covariance matrices C_{ij} must be evaluated. This can become computationally prohibitive if the number of terms in the sum (m) is large.

4.2 Optimizing Modal Performance

Like Gaul, optimizing modal control performance using Eq. (4-14) is divided into three parts:

1. Optimizing control bandwidths for a fixed modal basis and set of reconstruction matrices E_i;
2. Optimizing the reconstruction matrices E_i; and
3. Optimizing the modal basis itself.

Step number 1 is equivalent to modal control as currently implemented for conventional AO systems. Steps 2 and 3 are generalizations which may prove useful for MCAO.

On account of Eq. (4-1)–(4-3), the projection operators P_i may be written in the form

$$P_i = U D_i U^T, \tag{4-16}$$

where U is a unitary matrix which is common for all P_i, and the D_i's are diagonal, $\{0,1\}$-valued matrices with $\sum_i D_i = I$. The columns of U are the elements of the modal basis set, and mode number j is controlled at bandwidth i when $(D_i)_{(j,j)} = 1$. Note that m, the number of projection operators P_i, corresponds to the number of possible control bandwidths, and is not necessarily the same as $\dim(U)$, the number of elements in the modal basis. For numerical computations m and the temporal filters $k_1(\nu), \ldots, k_m(\nu)$ should be selected to adequately sample the range of bandwidths of interest, so that a discrete optimization performed over this finite set of choices will yield results which are similar to the fully optimized value.

Substituting Eq. (4-16) into Eq. (4-14) and applying the $U^T U = I$ and $\mathrm{trace}(MN) = \mathrm{trace}(NM)$ relationships yields the result

$$\begin{aligned} \left\langle \sigma^2 \right\rangle &= \sigma_f^2 + \sum_i \mathrm{trace}(D_i U^T M_i U) \\ &= \sigma_f^2 + \sum_i \sum_j (D_i U^T M_i U)_{(j,j)}. \end{aligned} \tag{4-17}$$

Since each D_i is diagonal and $\{0,1\}$-valued, the value of Eq. (4-17) can be minimized by setting $(D_i)_{(j,j)} = 1$ precisely when $(U^T M_i U)_{(j,j)}$ is the minimum of $(U^T M_k U)_{(j,j)}$ over all k. In other words,

$$\min_{\{D_i\}} \left\langle \sigma^2 \right\rangle = \sigma_f^2 + \sum_j \min_i (U^T M_i U)_{(j,j)}, \tag{4-18}$$

where the minimum on the left-hand-side is taken over all sets of diagonal, $\{0,1\}$-valued matrices D_i with $\sum_i D_i = 1$. Eq. (4-18) describes the performance of modal control when control bandwidths are optimized (over a discrete set of values) for a fixed modal basis and choice of wave front reconstruction matrices.

To optimize the reconstruction matrices E_i, note the matrix M_i defined in Eq. (4-15) is just the covariance matrix of the residual wave front errors for nodal control using the matrix E_i and the temporal filter $k_i(\nu)$. It follows that

$$(U^T M_i U)_{(j,j)} = \left|\left| \left(U^T (x - E_i y_i)\right)_{(j)} \right|\right|^2, \tag{4-19}$$

which will be minimized if E_i is choosen to be the optimal reconstructor for this bandwidth. Therefore

$$\min_{\{E_i\}} \min_{\{D_i\}} \left\langle \sigma^2 \right\rangle = \sigma_f^2 + \sum_j \min_i (U^T \mathcal{M}_i U)_{(j,j)}, \tag{4-20}$$

where $\mathcal{M}$ is the covariance matrix of residual phase errors for the optimal nodal reconstructor with the temporal filter $k_i(\nu)$:

$$\mathcal{M}_i = A - B_i C_{ii}^{-1} B_i^T + (I - B_i C_{ii}^{-1} G)(G^T C_{ii}^{-1} G)^{-1} (I - B_i C_{ii}^{-1} G)^T. \tag{4-21}$$

Finally, the global minimum σ_*^2 for the phase variance is achieved by minimizing Eq. (4-20) over the choice of unitary matrix U, with the result

$$\begin{aligned}\sigma_*^2 &= \min_U \min_{\{E_i\}} \min_{\{D_i\}} \left\langle \sigma^2 \right\rangle \\ &= \sigma_f^2 + \min_U \sum_j \min_i (U^T \mathcal{M}_i U)_{(j,j)}. \end{aligned} \tag{4-22}$$

Recall that optimization over U corresponds to optimizing the orthornormal basis set for modal control. Iterative, nonlinear search algorithms for determining the optimal U have been presented previously [2]. These algorithms would be computationally impractical for MCAO if modal control were applied to the full space of DM actuator commands, but this is not an issue for the low-dimensional subspace controlled by NGS WFS measurements.

5 Partially Decoupled NGS/LGS Control for MCAO

The control algorithm proposed for MCAO is a combination of the methods described in the preceeding two sections. The space of DM actuator commands is decomposed into LGS- and NGS-controlled subspaces. The NGS-controlled subspace is spanned by the tilt- and tilt anisoplanatism modes which are unsensed or very weakly sensed by the LGS WFS's. The high-order LGS subspace is controlled using a nodal algorithm, while modal control is used for the low-order NGS subspace. Fig. 3 is a block diagram of the control algorithm. The NGS and LGS control loops are not entirely decoupled, since residual errors in the LGS-controlled subspace do couple into the NGS WFS measurements. The remainder of this section evaluates the integrated performance of the two loops, and describes two approaches to minimizing the extent of the cross coupling.

The control law corresponding to Fig. 3 is described by the equation

$$\begin{pmatrix} c_l(\nu) \\ c_n(\nu) \end{pmatrix} = \begin{pmatrix} k_0(\nu)E_0 & 0 \\ 0 & \sum_i k_i(\nu) P_i E_i \end{pmatrix} \left[\begin{pmatrix} s_l(\nu) \\ s_n(\nu) \end{pmatrix} - \begin{pmatrix} G_{ll} & G_{ln} \\ G_{nl} & G_{nn} \end{pmatrix} \begin{pmatrix} c_l(\nu) \\ c_n(\nu) \end{pmatrix} \right]. \tag{5-1}$$

Here c_l is the LGS component of the DM actuator command vector, c_n is the NGS component, and s_l and s_n are the LGS and NGS components of the WFS measurement vector. The DM-to-WFS influence matrix G is divided into four blocks corresponding to the LGS and NGS components of the two vectors. Note that for an ideal system the matrix G_{ln} would be 0, since the LGS measurements are insensitive to tilt and tilt anisoplanatism. In practice G_{ln} can contain small nonzero elements due to fitting error if the DM approximations to these modes are inexact.

To obtain a usable expression for the actuator command vector $c(\nu)$, we restrict attention to reconstruction matrices which satisfy the constraints

$$E_0 G_{ll} = I, \tag{5-2}$$

$$E_i G_{nn} = I, \tag{5-3}$$

$$E_0 G_{ln} = 0 \tag{5-4}$$

Eq.'s (5-2) and (5-3) have been introduced previously, and two methods to achieve Eq. (5-4) for nonzero G_{ln} will be presented at the end of this section. With the aid of these conditions Eq. (5-1) becomes

$$\begin{pmatrix} [1+k_0(\nu)]I & 0 \\ \sum_i k_i(\nu) P_i E_i G_{nl} & I + \sum_i k_i(\nu) P_i \end{pmatrix} \begin{pmatrix} c_l(\nu) \\ c_n(\nu) \end{pmatrix} = \begin{pmatrix} k_0(\nu)E_0 & 0 \\ 0 & \sum_i k_i(\nu) P_i E_i \end{pmatrix} \begin{pmatrix} s_l(\nu) \\ s_n(\nu) \end{pmatrix}. \tag{5-5}$$

On account of Eq. (5-4), the LGS control loop is completely decoupled from the NGS component of the DM actuator commands. As in section 3, the dynamics of the LGS loop are described by the equations

$$c_l = E_0 y_l, \tag{5-6}$$

$$y_l(\nu) = \left[\frac{k_0(\nu)}{1+k_0(\nu)} \right] s_l(\nu). \tag{5-7}$$

The performance of the LGS control loop can now be evaluated and optimized as before.

Rearranging the second row of Eq. (5-5) and substituting Eq. (5-6) for c_l yields the result

$$c_n(\nu) = \left[I + \sum_i k_i(\nu) P_i \right]^{-1} \sum_i k_i(\nu) P_i E_i \left[s_n(\nu) - G_{nl} E_0 y_l(\nu) \right] \tag{5-8}$$

for the dynamics of the NGS control loop. Applying Eq.'s (4-1)–(4-3) for the properties of the projection operators P_i yields

$$c_n = \sum_i P_i E_i \widetilde{y}_i, \tag{5-9}$$

where the temporally filtered NGS WFS measurement vector $\widetilde{y}_i(\nu)$ is described by the equation

$$\begin{aligned} \widetilde{y}_i(\nu) &= \left[\frac{k_i(\nu)}{1 + k_i(\nu)} \right] \left[s_n(\nu) - G_{nl} E_0 y_l(\nu) \right] \\ &= \left[\frac{k_i(\nu)}{1 + k_i(\nu)} \right] s_n(\nu) - G_{nl} E_0 \left\{ \left[\frac{k_i(\nu) k_0(\nu)}{(1 + k_i(\nu))(1 + k_0(\nu))} \right] s_l(\nu) \right\}. \end{aligned} \tag{5-10}$$

The second term in this expression describes how the LGS component of the DM actuator command couples into the NGS control loop. Assuming that the LGS control loop compensates for most of the higher-order wave front distortion, the final term in Eq. (5-10) will improve the accuracy of the NGS tilt measurement $\widetilde{y}_i$. In a conventional LGS AO system, for example, the higher order DM correction reduces the aliasing of coma into the NGS tip/tilt measurement.

Performance evaluation for the modal NGS control loop now proceeds as in section 4, with $y_i(\nu)$ replaced with $\widetilde{y}(\nu)$. Computing the covariance matrices B_i and C_{ii} is somewhat more difficult, since the definition of $\widetilde{y}_i(\nu)$ contains two different temporal filters. The overall performance of the MCAO system can be obtained by summing the expected residual variances for the NGS and LGS control loops.

5.1 Insuring $E_0 G_{ln} = 0$

There are two approaches to insuring that $E_0 G_{ln} = 0$ so that the LGS and NGS control loops can be decoupled as described above. For the first approach, assume that the space of DM actuator commands has already been decomposed into LGS and NGS components, and that $G_{ln} \neq 0$ due to DM fitting error. We can preprocess the LGS WFS measurement vector y_l, so that effectively $G_{ln} = 0$, by nulling the component of y_l in the range space of G_{ln}. This is accomplished by the projection operator

$$y_l \rightarrow [I - G_{ln}(G_{ln}^T W_l^{-1} G_{ln})^{-1} G_{ln}^T W_l^{-1}] y_l, \tag{5-11}$$

where W_l is the noise covariance matrix for the LGS WFS measurements. This preprocessing is highly analogous to the full aperture tip/tilt removal used in conventional LGS AO systems on account of LGS position uncertainty. Since the rank of G_{ln} is equal to the small number of NGS-controlled modes, one expects that the projection in Eq. (5-11) should not eliminate much information from the LGS WFS measurement vector.

With y_l redefined as above, the new values of G_{ll} and G_{ln} become

$$G_{ll} \rightarrow [I - G_{ln}(G_{ln}^T W_l^{-1} G_{ln})^{-1} G_{ln}^T W_l^{-1}] G_{ll}, \tag{5-12}$$

$$\begin{aligned} G_{ln} &\rightarrow [I - G_{ln}(G_{ln}^T W_l^{-1} G_{ln})^{-1} G_{ln}^T W_l^{-1}] G_{ln} \\ &= 0, \end{aligned} \tag{5-13}$$

so that $E_0 G_{ln} = 0$ as required. Note that the new definition of y_l must also be used to compute the covariance matrices B and C when evaluating the LGS control algorithm.

As a second option for insuring $E_0 G_{ln} = 0$, suppose that an integrated MCAO reconstruction matrix E has already been computed with $EG = I$. With E and G decomposed into NGS and LGS WFS components this constraint may be written as.

$$\begin{pmatrix} E_{\bullet l} & E_{\bullet n} \end{pmatrix} \begin{pmatrix} G_{l\bullet} \\ G_{n\bullet} \end{pmatrix} = I. \tag{5-14}$$

The bullets in the subscripts are intended to indicate that the matrix E is decomposed by columns, while G is decomposed by rows. Next, compute a unitary matrix U of the form

$$U = \begin{pmatrix} U_l & U_n \end{pmatrix}, \tag{5-15}$$

where the columns of U_n are an orthogonal basis for the span of the columns of $E_{\bullet n}$, and the column of U_l extend this basis to the full DM actuator command space. Define the NGS-controlled subspace as the span of U_n, and the LGS-controlled subspace as the span of U_l. We have $U_l^T E_{\bullet n} = 0$ because the columns of U_l are orthogonal to the columns of U_n, and the columns of U_n and $E_{\bullet n}$ span the same subspace. Pre- and post-multiplying Eq. (5-14) by U^T and U therefore yields

$$\begin{pmatrix} U_l^T E_{\bullet l} & 0 \\ U_n^T E_{\bullet l} & U_n^T E_{\bullet n} \end{pmatrix} \begin{pmatrix} G_{l\bullet} U_l & G_{l\bullet} U_n \\ G_{n\bullet} U_l & G_{n\bullet} U_n \end{pmatrix} = \begin{pmatrix} I & 0 \\ 0 & I \end{pmatrix}. \tag{5-16}$$

Since $G_{l\bullet} U_l = G_{ll}$ and $G_{l\bullet} U_n = G_{ln}$ for this definition of the NGS- and LGS-controlled subspaces, the top row of Eq. (5-16) is equivalent to Eq.'s (5-2) and (5-4) for E_0 defined by the formula

$$E_0 = U_l^T E_{\bullet l}. \tag{5-17}$$

It is worth noting that these two methods have different computation requirements. For the first approach the matrix E_0 is independent of the NGS constellation, while for the second technique this large matrix must be recomputed for each new science field. Also, for the second approach the dimension of the NGS-controlled subspace will be twice the number of NGS, so that one or more additional modes will be included beyond tip/tilt and tilt anisoplanatism.

6 Sample Numerical Results

This section presents sample results on MCAO performance derived using the partially decoupled LGS/NGS control algorithm described above.

6.1 Scenario Description

The first-order parameters for the MCAO system and observing scenario are summarized in Table 1. These values correpond closely to the proposed MCAO system for Gemini-South, except that the orders of the WFS's and DM's have been reduced from 16×16 to 12×12 to relax computation requirements. The sampling rate for all WFS's is fixed at 800 Hz, and the -3 dB closed-loop control bandwidth for the LGS control loop is a fairly conservative 32.2 Hz. The modal gains for the NGS control loop are taken from the set of 11 values $\{0.01, 0.02, 0.03, 0.05, 0.07, 0.10, 0.20, 0.30, 0.50, 0.70, 1.00\}$, and correspond to closed-loop bandwidths between about 1.27 and 92.0 Hz. Note that the control law used for the LGS modes includes one additional full frame of latency to account for readout of the LGS WFS CCD array, while the control law for NGS modes assumes quad detector APD tip/tilt sensors with neglegible readout time.

Table 2 lists the parameters used to model WFS measurement accuracy. The LGS parameters match those used in an earlier report [3], and correspond to 8.2 Watts per guide star for an unsaturated CW laser source mounted on the Gemini telescope. The NGS parameters are based upon experience at CFHT, with 4 sky background values corresponding to 80%, 50%, 20%, and bright time conditions at Mauna Kea. The formulas used to related LGS WFS signal-to-noise and LGS spot size to tilt measurement accuracy assume

Aperture diameter	8.0 m
Obscuration ratio	0.152 (linear)
Observing bands	J, H, K
Zenith Angle	0 degrees
Science field	1 arc minute square (see Fig. 4)
Turbulence/wind profiles	Median Cerro Pachon (see Table 3)
Turbulence spectrum	Kolmogorov, infinite outer scale
Windshake tip/tilt jitter PSD	Typical Mauna Kea (see Eq. (6-3))
DM conjugate ranges	0, 4.5, 9.0 km
DM actuator pitches	0.667, 0.667, 1.333 m
Number of LGS	5 (see Fig. 4)
LGS WFS order	12 by 12
Number of NGS	3 (see Fig. 4)
NGS WFS order	1 by 1 (tip/tilt)
WFS sampling rate	800 Hz
Control dynamics, LGS modes	$c_{n+1} = \frac{1}{2}(c_n + c_{n-1}) + \frac{1}{2}e_{n-1}$
Control dynamics, NGS modes	$c_{n+1} = c_n + k_i e_n$

Table 1: AO system and observing scenario parameters for numerical results
Here c_n is the DM actuator command vector at cycle number n, and e_n is the output of the matrix multiply wave front reconstructor. See the text of Section 6 for further details.

quadrant detector tilt sensing, and have been described previously [3]. The NGS tilt measurement error σ_θ for a full-aperture quadrant detector tip/tilt sensor has been computed using the formulas

$$\sigma_\theta = 0.57\frac{(\lambda/r_0)}{\mathrm{SNR}} \tag{6-1}$$

$$\mathrm{SNR} = N_p/\sqrt{N_p + 4N_b}, \tag{6-2}$$

where σ_θ is expressed in radians of tilt, λ is the mean wavelength of the NGS wave front sensing passband, N_p is the mean number of signal photodetection events per frame, and N_b is the mean number of background photodetection events per pixel per frame. Eq. (6-1) assumes that the full aperture, visible images of the NGS are not appreciably sharpened by the MCAO system.

Fig. 4 illustrates the one LGS and three NGS constellations considered here. The LGS constellation consists of 5 guide stars located at the center and slightly outside the four corners of the 1 arc minute square science field. The first, and most favorable, NGS constellation includes three guide stars located at the vertices of an equilateral triangle with a base equal to 0.87 arc minute. The center of gravity of this triangle coincides with the center of the science field. The second constellation scales the equilateral triangle by a factor of one-half, and this smaller triangle is displaced to one side of the science field for the third constellation. These three cases provide a qualitative indication of how the distribution of natural guide stars impacts MCAO performance, but additional cases would need to be considered to develop quantitative models for this effect.

Table 3 lists the discrete seven-layer approximation to the median Cerro Pachon turbulence profile used for these calculations. The PSD assumed for the total (two-axis) windshake-induced tip/tilt jitter is given by the equation

$$\mathrm{PSD}(f) = \begin{cases} 2.686 \times 10^{-4} \text{ arc sec}^2/\text{Hz} & \text{for } f \le 6.4\,\text{Hz}, \\ 7.560 \times 10^{2} f^{-8} \text{ arc sec}^2/\text{Hz} & \text{otherwise.} \end{cases} \tag{6-3}$$

Note that this is a model PSD for typical windshake jitter at *Gemini-North*, and the results presented here must be considered prelimenary pending further computations using more exact windshake values.

NGS zeropoint at WFS detector	0.557×10^{12} PDE/sec
NGS sky brightness, mag/sec^2	
80%	21.51
50%	21.03
20%	20.18
Bright time	18.80
Mean NGS wavelength	0.7 μm
NGS WFS pixel size	0.5 arc sec
NGS WFS detector read noise	none
LGS zeropoint at WFS detector	0.201×10^{11} PDE/m^2/sec
LGS magnitude	10.5
LGS wavelength	0.589 μm
LGS launch configuation	On-axis gaussian beam with 0.3 m $1/e^2$ diameter
LGS laser beam quality	1.5 times diffraction limited
Sodium laser range	90–100 km
LGS WFS lenslet aberrations	Gaussian blur, 0.25 λ/d FWHM
LGS WFS pixel size	1.0 arc sec
LGS WFS pixel charge diffusion	Gaussian blur, 0.25 pixel FWHM
LGS WFS detector read noise	6 e$_-$

Table 2: WFS radiometry parameters for numerical results
The LGS WFS lenslet aberrations are characterized in terms of a Gaussian transfer function, with λ/d being the diffraction-limited spot size associated with the WFS subaperture width d and the LGS wavelength λ. See the text of Section 6 for further details.

Finally, the theory described in the preceeding sections characterizes MCAO performance in terms of a field-of-view-averaged mean-square phase error, but it is more useful to work in terms of Strehl ratios when evaluating NGS magnitude limits. Since the NGS-controlled modes in a MCAO system consist of tilt and tilt anisoplanatism, the effect of residual errors in these modes will be image motion at any given point in the field-of-view. If we make the assumption that these tip/tilt errors are isotropic and uniformly distributed, a good approximation for the associated reduction in Strehl ratio is the formula

$$S = \frac{1}{1 + \sigma^2}. \tag{6-4}$$

Here S is the Strehl ratio reduction due to residual errors in the NGS-controlled modes alone, and σ^2 is the mean-square phase error in these modes. Eq. (6-3) is only an approximation however, since the tip/tilt errors will not be uniformly distributed across the field. More exact results could be obtained by computing the full second-order statistics of the residual NGS-controlled modes, but (as described in section 4.1) this refinement would increase computation requirements considerably.

Before proceeding to the results subsection, it is worth repeating the areas where this test case problem diverges from the parameters proposed for MCAO on Gemini-South:

1. Reduced orders for the LGS WFS's and DM's;
2. Preliminary SNR estimates for the NGS WFS's;
3. Preliminary estimates for windshake-induced tip/tilt jitter;
4. LGS locations slightly outside of the 1 arc minute science field; and
5. Approximate values for the Cerro Pachon wind profile.

Layer	h, meters	Fractional $C_n^2(h)$	Windspeed, m/sec
1	0	0.646	5
2	1800	0.078	10
3	3300	0.119	15
4	5800	0.035	20
5	7400	0.025	30
6	13100	0.080	20
7	15800	0.015	10

Table 3: Cerro Pachon turbulence and windspeed profiles
These profiles are discrete fits to the median conditions measured during the Cerro Pachon site survey [5]. The corrresponding values of r_0 and θ_0 at 0.5 microns are 0.166 cm and 2.74 μrad.

Item number one was an intentional choice to reduce computation requirements, items two and three use the best estimates presently available, and items four and five are the results of goofs not discovered until after the calculations were completed. We assert that none of these differences is significant enough to invalidate the basic results of the analysis.

6.2 Results

Fig. 5 illustrates MCAO performance for NGS constellation (b) and the idealized case of no windshake-induced tip/tilt jitter. The second method outlined in section 5.1 has been used to decouple the NGS and LGS control loops. The upper left subfigure plots the mean-square phase variance at 0.5 microns as a function of NGS magnitude for the four different sky background levels listed in Table 2. The magnitudes of the three NGS are assumed to be equal. The remaining three subplots in Fig. 5 translate these phase variances into Strehl ratios in J, H, and K bands using Eq. (6-4). For the 80% sky background, the limiting NGS magnitude for a 50% Strehl ratio reduction in H band is about 20.3. For the 20% background the value is 19.8, and for bright time it is approximately 19.4. The limiting NGS magnitude is about 18 for an 80% Strehl in H, and is less sensitive to sky brightness. For very bright NGS, the residual phase variance for the partially decoupled LGS/NGS control algorithm asymptotes to a value which is actually smaller by about 0.4 rad^2 than the variance for an integrated nodal control algorithm for all DM degrees-of-freedom.[4]

Results for NGS constellation (b) with windshake-induced tip/tilt jitter included are presented in Fig.'s 6 and 7. For Fig. 6 the tip/tilt jitter is assumed to be excited along a single axis ("1-d windshake"), while in Fig. 7 the jitter is uniformly distributed in x and y ("2-d windshake"). Results for the later cases are slightly poorer and will be used as a conservative lower bound. The limiting NGS magnitude for a 50% Strehl ratio reduction in H band is now 19.2 for the 80% sky background, 18.9 for 20%, and 18.6 for bright time. These values have increased by approximately one magnitude from the corresponding limits without windshake, but they should be considered preliminary until a more exact windshake jitter spectrum is available. These results do indicate that MCAO is no more sensitive to windshake than conventional LGS AO [4].

The results in Fig.'s 5–7 assume three NGS of equal magnitude. Fig. 8 illustrates MCAO performance as a function of the magnitude of a single NGS when the magnitudes of the remaining two NGS are fixed at 20. Performance asymptotes to a disappointing value for a NGS brighter than about magnitude 18. Heuristically, this result occurs because tilt anisoplanatism must be estimated based upon the apparent separations between the bright NGS and the two magnitude 20 NGS, and the signal levels for the two dim stars are too low to make these measurement with good accuracy at a high sampling rate.

[4] This last result is unexpected, but not actually contradictory. Neither of these two control algorithms is optimal due to the $EG = I$ constraints, which are not identical for the two approaches. The performance of both algorithms is inferior to the optimal estimator without closed loop constraints by about 1.5–2.0 rad^2, as required.

Fig.'s 9 and 10 plot similar results for the two NGS constellations illustrated in parts (c) and (d) of Fig. 4. As with Fig. 7 for NGS constellation (b), these values include the effect of windshake and assume that all three NGS are of equal magnitude. For constellation (c) (Fig. 9), the limiting magnitudes for a 50% Strehl ratio reduction in H band ranges from about 18.5 for 80% sky background to about 18.1 for bright time. These values are about 0.5 to 0.7 magnitudes brighter than the corresponding results for constellation (b) in Fig. 7, since the smaller separations between the stars in constellation (c) imply reduced measurement sensitivity for tilt anisoplanatism. For bright guide stars, the asymptotic Strehl ratios for constellations one and two are virtually identical. For NGS constellation (d) the limiting magnitudes are reduced further by about 0.2–0.3. Because this constellation is decentered the NGS tip/tilt measurements associated with tilt and tilt anisoplanatism are cross-coupled, and somewhat higher SNR's are required for the same estimation accuracy. The asymptotic performance with bright NGS also degrades modestly for constellation (d), presumably due to increased spatial aliasing of the residual errors in the LGS-controlled modes. The residual phase variance is increased by about 0.56 rad^2 at a wavelength of 0.5 μm, which corresponds to a Strehl ratio factor of about 0.95 (0.97) in H (K) band.

Finally, Fig. 11 replots results from Fig.'s 7, 9, and 10 for the 80% sky background to highlight the variations in MCAO performance with respect to the NGS constellation. Although the space of possible constellations containing 3 NGS is 9-dimensional (x, y, and magnitude for each guidestar, with some symmetries), we hope to develop parameteric fits to these results which will enable more precise sky coverage calculations.

7 Summary and Plans

In this report we have described a method for developing and evaluating practical wave front reconstruction algorithms for combined LGS/NGS MCAO systems. The space of DM actuator commands is decomposed into separate LGS- and NGS-controlled subspaces. The high-dimensional LGS-controlled subspace is compensated using nodal control with a fixed reconstruction matrix. The low-dimensional NGS-controlled space is compensated using modal control, which may be adapted in real time to match atmospheric conditions and the particulars of the NGS constellation. Proper selection of the two subspaces decouples the LGS control loop from the residual errors in the NGS-controlled subspace. Residual errors in the LGS-controlled subspace alias into the NGS-controlled loop and act as a source of correlated measurement noise, but the resulting estimation errors will be small if the performance of the LGS control loop is satisfactory.

The overall mean-square residual phase error associated with this control algorithm can be evaluated analytically as a function of MCAO system parameters and atmospheric conditions.

Performance estimates for sample problems derived from the proposed MCAO system for Gemini-South indicate that

- For bright NGS, the performance of the decoupled control algorithm is effectively the same as the optimal nodal control algorithm;
- The NGS magnitude limits for a 50% Strehl ratio reduction in H band correspond to scientifically useful levels of sky coverage;
- MCAO performance does not vary drastically with the spatial arrangement of the NGS. The above limiting magnitude is still in the range from 18 to 18.5 for 3 NGS separated by as little as 0.43 arc minutes located anywhere in the science field-of-view;
- MCAO sensitivity to windshake-induced tip/tilt jitter is comparible to conventional LGS AO; and
- MCAO performance is also not a dramatic function of the sky background, with useful results still possible under 20% conditions.

Additional work is certainly possible to more carefully characterize potential MCAO performance for Gemini-South. Some the parameters which could be matched more precisely to this system and site include

- The order the the DM's and WFS's;
- The locations of the LGS relative to the science field-of-view;
- The atmospheric wind profile;
- The windshake-induced tip/tilt jitter PSD;
- LGS and NGS radiometry; and
- Calculations for a wider range of atmospheric conditions and NGS constellations.

None of these adjustments appear significant enough to alter the conclusion that MCAO sky coverage will be large enough to be scientifically interesting. Finally, it is highly desirable to characterize how the variabilty of the compensated PSF depends upon the locations and magnitudes of the natural guide stars, but this information may, perhaps, be more easily obtained via simulations.

References

[1] B. L. Ellerbroek, "First-order performance evaluation of adaptive-optics systems for atmospheric turbulence compensation in extended-field-of-view astronomical telescopes," J. Opt. Soc. Am A **11**, 783–805 (1994).

[2] B. L. Ellerbroek, C. V. Loan, N. Pitsianis, and R. J. Plemmons, "Optimizing closed-loop adaptive-optics performance with use of multiple control bandwidths," J. Opt. Soc. Am A **11**, 2871–2886 (1994).

[3] B. L. Ellerbroek, "LGS AO and MCAO Performance as a Function of LGS Signal Level," Gemini Document RTP-AO-Gxxxx (2000).

[4] B. L. Ellerbroek and D. W. Tyler, "Adaptive optics sky coverage calculations for the Gemini-North telescope," Proc. Astron. Soc. Pac. **110**, 165-185 (1997).

[5] J. Vernin *et al.*, "1998 GEMINI SITE TESTING CAMPAIGN: Cerro Pachon and Cerro Tololo," Gemini Document RTP-AO-G0094 (2000).

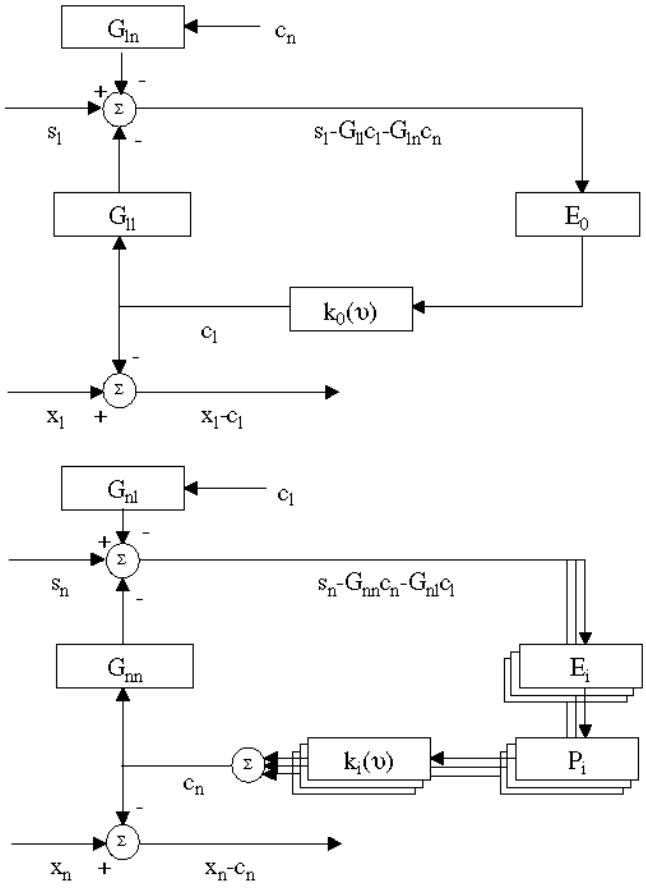

Figure 3: MCAO Control Block Diagram

The top half of the figure illustrates nodal control used for the LGS-corrected (l) component of the wave front distortion. The bottom half illustrates modal control for the NGS-corrected (n) component. The two-loops are potentially crosscoupled by the action of the DM-to-WFS interaction matrix G, unless care is taken in the definition of the two subspaces and the selection of the reconstruction matrices.

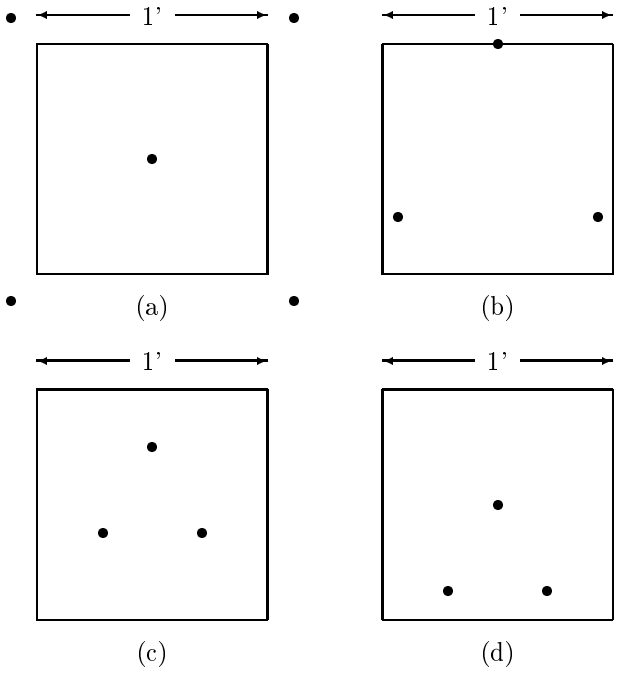

Figure 4: Guide star constellations for MCAO calculations
These schematics illustrate the fixed constellation of five higher-order LGS (a) and the three constellations of three tip/tilt NGS (b through d) considered in this section. The square box is the 1 arc minute square science field.

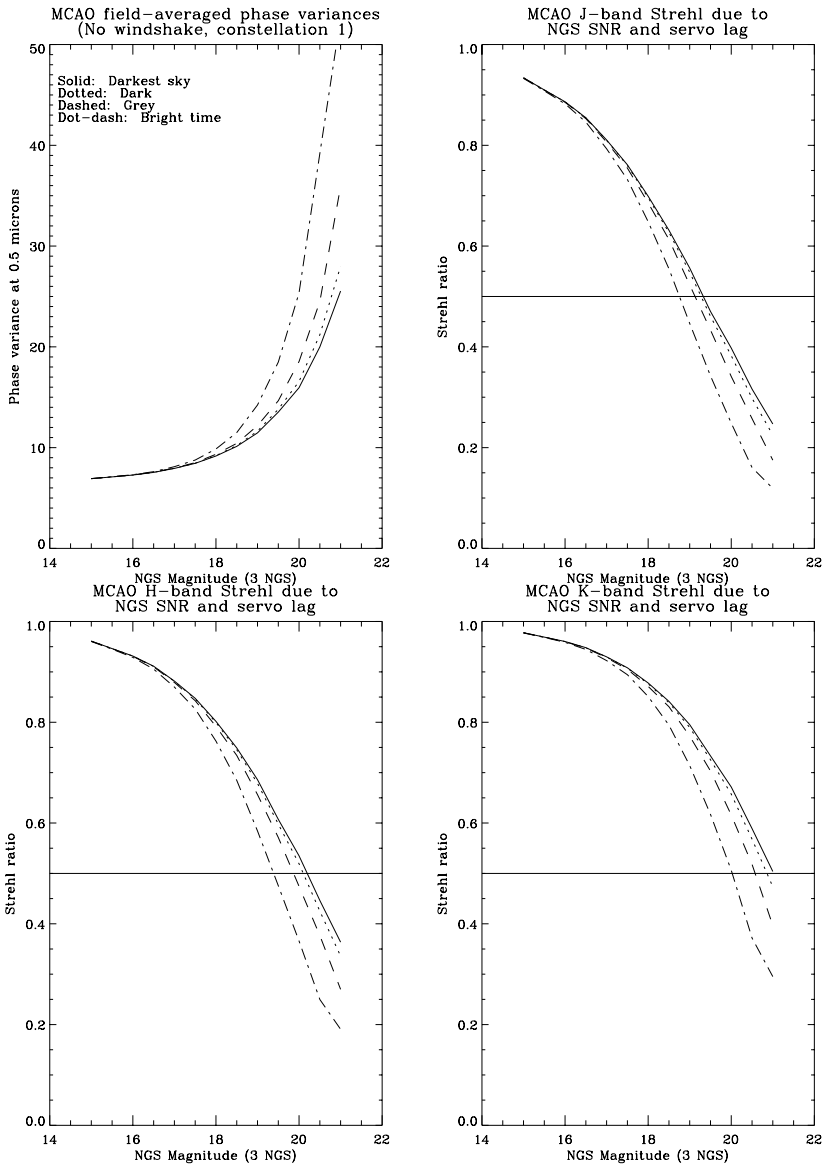

Figure 5: MCAO performance vs NGS magnitude without windshake

These results correspond to the MCAO and observing parameters listed in Table 1, with the locations of the three tip/tilt NGS within the science field as illustrated in Fig. 4b. The first subfigure plots MCAO performance in terms of the residual phase variance at 0.5 microns averaged over the 1 square arc minute field-of-view. All three NGS are of equal magnitude. The remaining three subfigures plot the field-averaged Strehl ratio reductions in J, H, and K bands which can be associated with NGS measurement noise and servo lag for the NGS-controlled modes, as computed using Eq. (6-4)

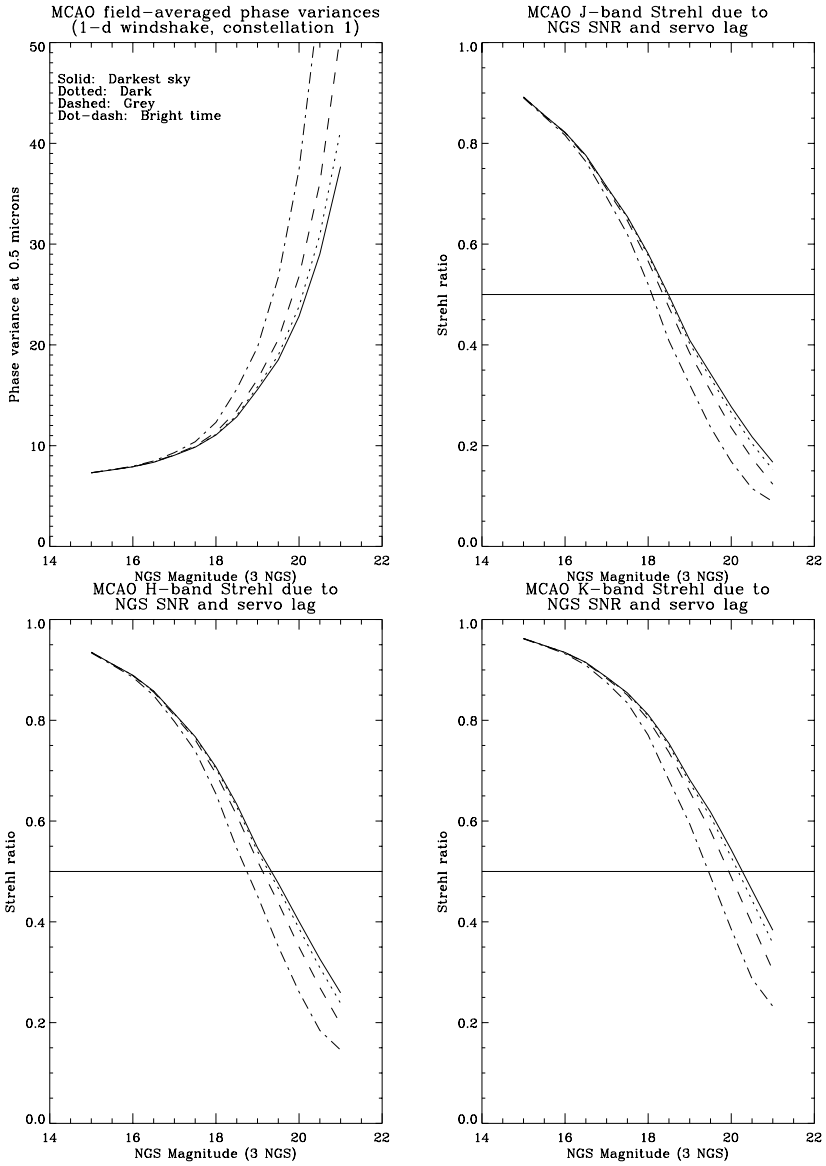

Figure 6: MCAO performance vs NGS magnitude with windshake in one dimension
This figure is similar to Fig. 5, except the windshake tip/tilt jitter described by Eq. (6-3) has been included in the analysis. The results have been averaged over one-dimensional tip/tilt jitter in both the x and y directions.

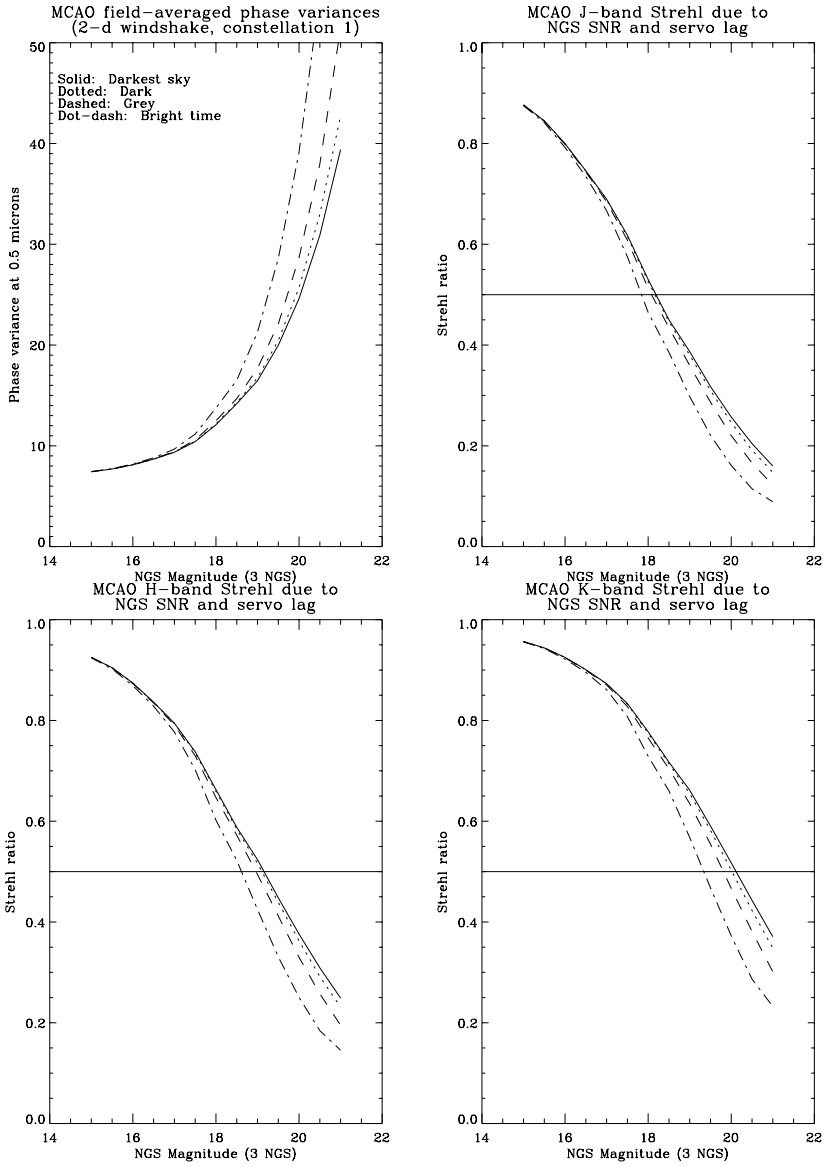

Figure 7: MCAO performance vs NGS magnitude with windshake in two dimensions
This figure is similar to Fig. 6, except that the windshake tip/tilt jitter is equally distributed between the x and y axes.

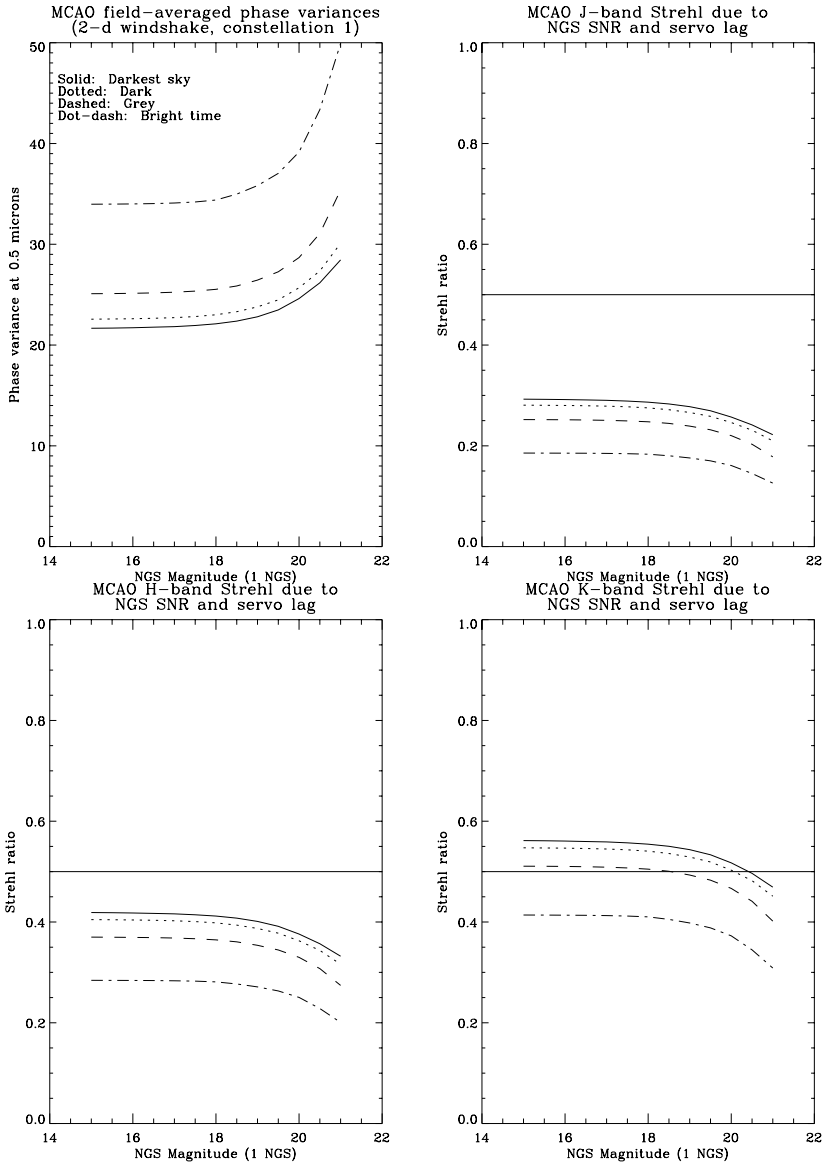

Figure 8: MCAO performance vs NGS magnitude with one bright star
This figure is similar to Fig. 6, except that only one of the three NGS used for tip/tilt sensing is of the indicated magnitude. The remaining two NGS are fixed at magnitude 20.

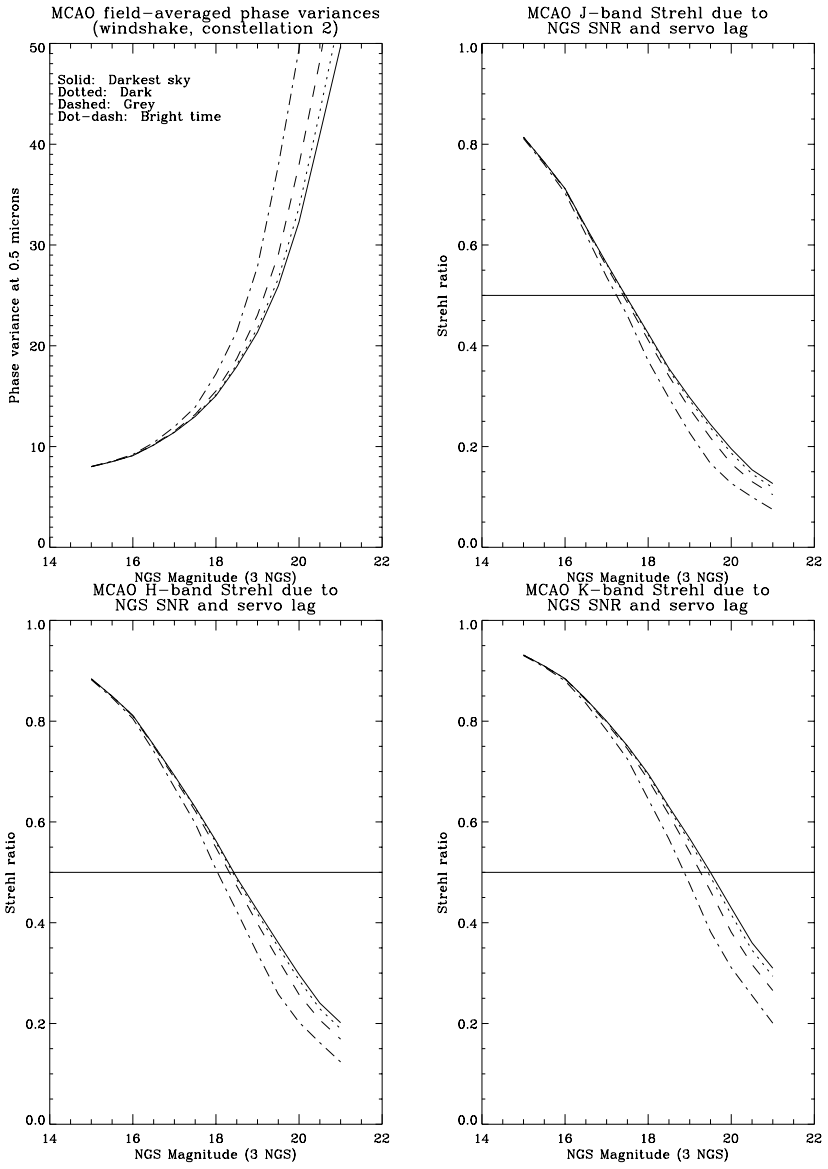

Figure 9: MCAO performance vs NGS magnitude for NGS constellation (c)
This figure is similar to Fig. 7, except that the NGS constellation used for tip/tilt sensing is as illustrated in Fig. 4c. The effect of windshake-induced tip/tilt jitter is included.

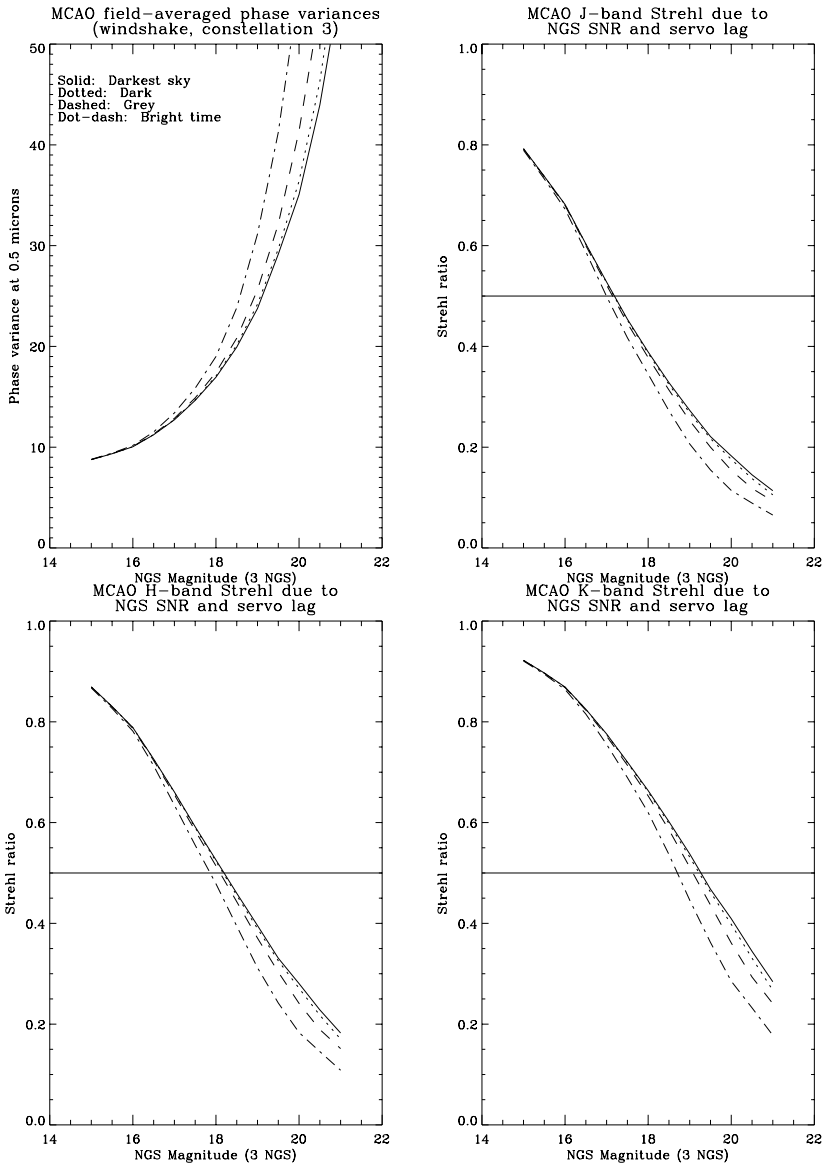

Figure 10: MCAO performance vs NGS magnitude for NGS constellation (d)
This figure is similar to Fig. 7, except that the NGS constellation used for tip/tilt sensing is as illustrated in Fig. 4d.

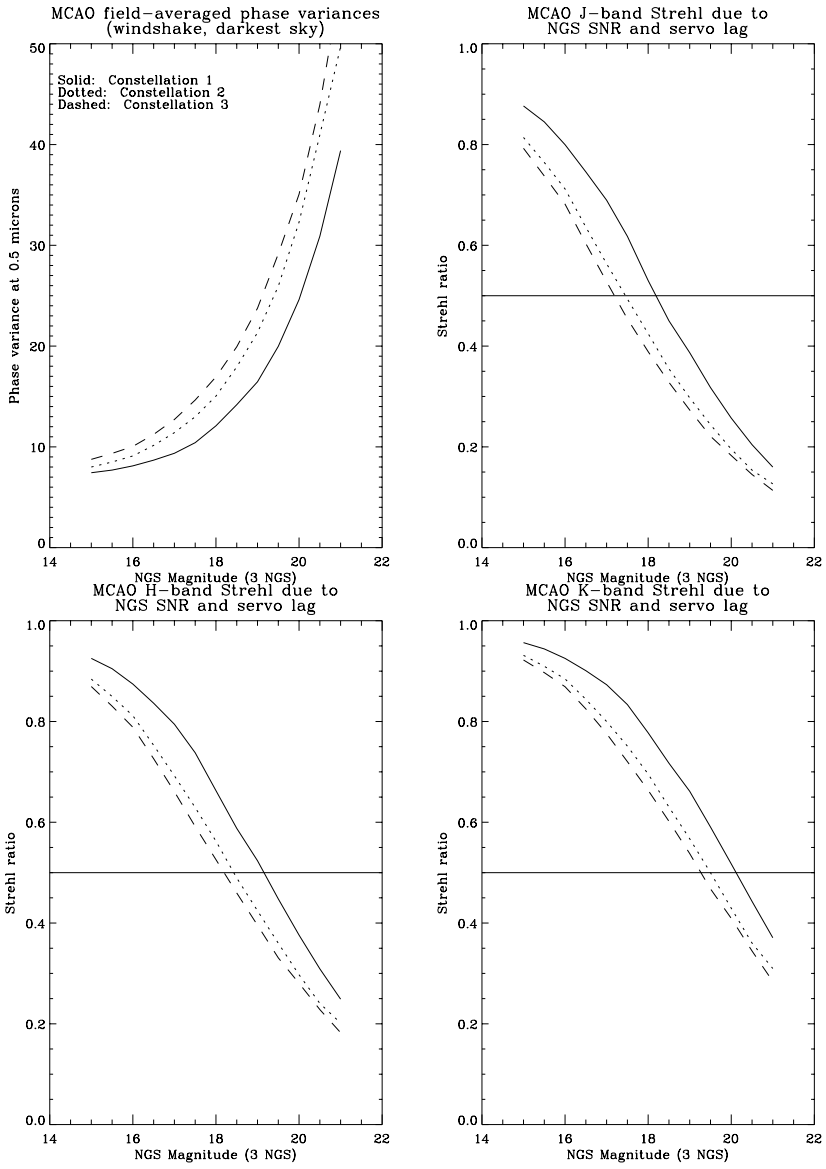

Figure 11: MCAO performance vs NGS magnitude and constellation

This figure replots results from Fig.'s 7, 9, and 10 for the 80% sky background to more clearly compare MCAO performance for the three different NGS constellations illustrated in Fig. 4.